



Article

# Zeolitic Imidazolate Framework Decorated Molybdenum Carbide Catalysts for Hydrodeoxygenation of Guaiacol to Phenol

Jintu Francis Kurisingal , Shinjae Lee, Jun Gyeong Lee and Kwangjin An \* 

School of Energy and Chemical Engineering, and Graduate School of Carbon Neutrality, Ulsan National Institute of Science and Technology (UNIST), Ulsan 44919, Republic of Korea

\* Correspondence: [kjan@unist.ac.kr](mailto:kjan@unist.ac.kr); Tel.: +82-52-217-2586

**Abstract:** Bimetallic zeolitic imidazolate framework (BMZIF)-decorated Mo carbide catalysts were designed for the catalytic hydrodeoxygenation of guaiacol to produce phenol with high selectivity. A uniform layer of BMZIF was systematically coated onto the surface of the MoO<sub>3</sub> nanorods. During carbonization at 700 °C for 4 h, BMZIF generated active species (ZnO, CoO) on highly dispersed N-doped carbons, creating a porous shell structure. Simultaneously, the MoO<sub>3</sub> nanorod was transformed into the Mo<sub>2</sub>C phase. The resulting core@shell type Mo<sub>2</sub>C@BMZIF-700 °C (4 h) catalyst promoted a 97% guaiacol conversion and 70% phenol selectivity under 4 MPa of H<sub>2</sub> at 330 °C for 4 h, which was not achieved by other supported catalysts. The catalyst also showed excellent selective cleavage of the methoxy group of lignin derivatives (syringol and vanillin), which makes it suitable for selective demethoxylation in future biomass catalysis. Moreover, it exhibits excellent recyclability and stability without changing the structure or active species.

**Keywords:** biomass; hydrogenation; phenol; metal-organic frameworks; zeolitic imidazolate framework



**Citation:** Kurisingal, J.F.; Lee, S.; Lee, J.G.; An, K. Zeolitic Imidazolate Framework Decorated Molybdenum Carbide Catalysts for Hydrodeoxygenation of Guaiacol to Phenol. *Catalysts* **2022**, *12*, 1605. <https://doi.org/10.3390/catal12121605>

Academic Editors: Karine De Oliveira Vigier and Mickael Capron

Received: 7 November 2022

Accepted: 29 November 2022

Published: 7 December 2022

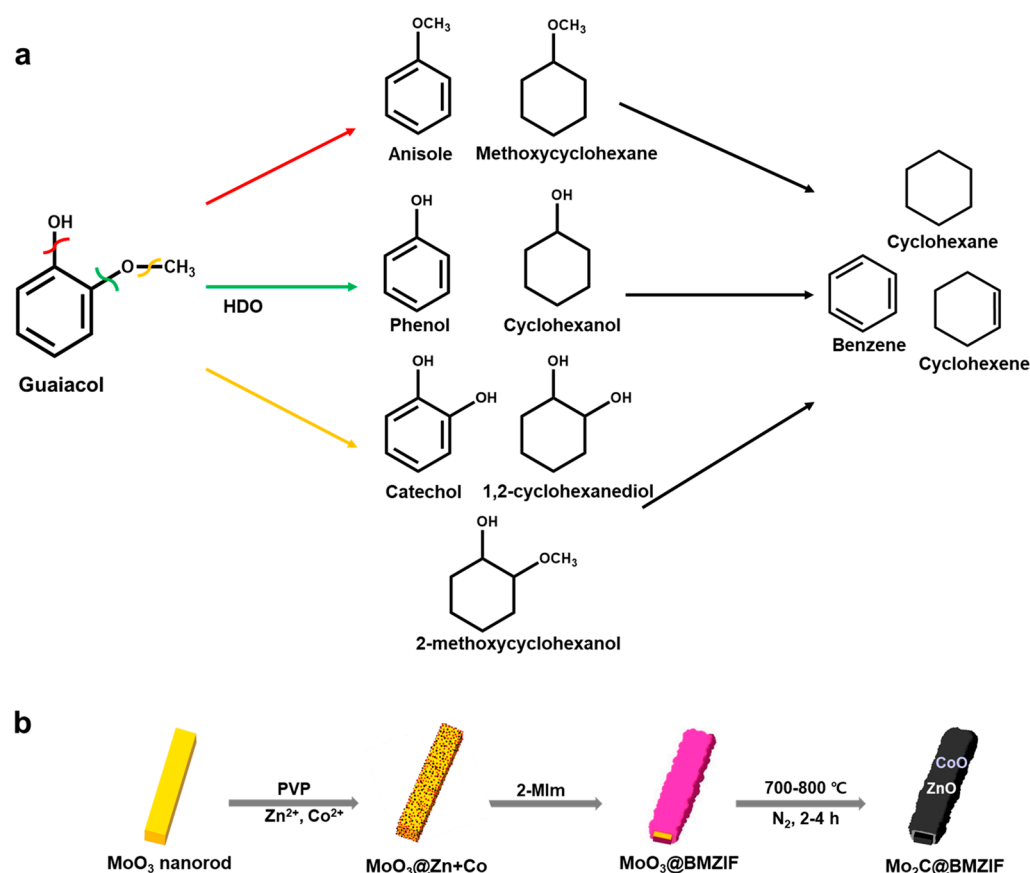
**Publisher's Note:** MDPI stays neutral with regard to jurisdictional claims in published maps and institutional affiliations.



**Copyright:** © 2022 by the authors. Licensee MDPI, Basel, Switzerland. This article is an open access article distributed under the terms and conditions of the Creative Commons Attribution (CC BY) license (<https://creativecommons.org/licenses/by/4.0/>).

## 1. Introduction

For sustainable and green chemistry, the use of lignocellulosic biomass has received increasing attention owing to the increasing energy demand and environmental issues worldwide [1–4]. Lignocellulosic biomass primarily consists of cellulose (40–50%), hemicelluloses (20–30%), and lignin (18–28%). Despite the cross-linked complex and recalcitrant structure of lignin, aromatic building blocks make it a promising starting material for producing valuable aromatic compounds [5–12]. A feasible and effective route for lignin valorization is the depolymerization of lignin followed by hydrodeoxygenation (HDO) into lignin-derived phenolic compounds [13]. Guaiacol (2-methoxyphenol, C<sub>7</sub>H<sub>8</sub>O<sub>2</sub>), one of the main compounds in lignin-derived bio-oil, can be used in HDO reactions to produce value-added chemicals (Scheme 1a). Guaiacol contains three different types of C–O bonds: phenolic (Ar–OH) and methoxy (Ar–O–CH<sub>3</sub>) groups. Since product selectivity varies depending on how the C–O bond is broken, it is essential to develop highly selective HDO catalysts [14–18]. The phenolic group of guaiacol is known to be more thermodynamically stable than the methoxy group, indicating that the cleavage of Ar–OCH<sub>3</sub> is more likely to produce phenol [19–22]. The production of phenol by selective HDO is highly valuable because of its high demand, rising market price, and low consumption of H<sub>2</sub> for production. Phenol is used as a major industrial intermediate to produce pesticides and polymers. In particular, phenol has been used to produce adipic acid to synthesize industrially valuable polymers, such as nylon 6,6 [23–25].



**Scheme 1.** (a) Schematic representation of the possible reaction pathways and products by catalytic HDO of guaiacol. (b) Schematic illustration of the synthesis of ZIF-decorated Mo carbide nanorods with a core@shell structure.

Numerous studies have been conducted to develop effective catalysts with high conversion and high product selectivity in the HDO of guaiacol. These catalysts include noble metals [26,27], non-noble metals [28–30], metal sulfides [20], phosphides [31], nitrides [32], and carbides. Although noble metal catalysts have high conversion rates, most products are low-value saturated aromatics, such as cyclohexanol and cyclohexane, by complete hydrogenation of the aromatic ring with oxygen removal. Mo-based catalysts (MoO<sub>3</sub>, Mo<sub>2</sub>C, Mo<sub>2</sub>N, and MoS<sub>2</sub>) have shown excellent catalytic activity and selectivity in the HDO reaction of guaiacol to produce phenolic compounds [33–41]. The Roman–Leshkov group investigated the bond dissociation energy of the relevant phenolic C–O bonds of lignin-derived model compounds using MoO<sub>3</sub>. However, the MoO<sub>3</sub>-catalyzed HDO of guaiacol showed 29.3% selectivity towards phenol with a 97.5% conversion under low H<sub>2</sub> pressure (1 bar) at 350 °C [42]. The Weckhuysen group reported phenol production from guaiacol over a sulfided CoMo/Al<sub>2</sub>O<sub>3</sub> catalyst with a phenol selectivity of 34% at 300 °C and 50 bar of H<sub>2</sub> [38]. They also reported Mo<sub>2</sub>C support on carbon nanofibers (CNFs) with enhanced phenol selectivity of more than 50% in 55 bars of H<sub>2</sub> at 350 °C [43]. Chang et al. investigated various metal catalysts supported on carbon [44]. They found that the Mo/C catalyst exhibited the best selectivity toward phenol (76.5%) in the HDO of guaiacol at 40 bars of H<sub>2</sub> at 400 °C. The partially reduced MoO<sub>x</sub> species were regarded as an active site for direct demethoxylation of guaiacol to form phenol. Cai et al. compared the HDO performance of guaiacol between activated carbon (AC)-supported MoO<sub>2</sub> and Mo<sub>2</sub>C [45]. They found that MoO<sub>2</sub>/AC showed much higher selectivity toward phenol (72.0%) than Mo<sub>2</sub>C/AC (28.9%) in 30 bars of H<sub>2</sub> at 300 °C. In contrast, Li et al. reported a graphite-encapsulated Mo-carbide core@shell catalyst (Mo<sub>2</sub>C@C), which showed 68.6% phenol selectivity in 28 bars of H<sub>2</sub> at 300 °C [46]. The DeSisto and Escalona group investigated the HDO of guaiacol using

various Mo<sub>2</sub>N-based catalysts. They revealed that the  $\gamma$ -Mo<sub>2</sub>N phase was the primary phase for the selective production of phenolic compounds [37,47,48].

Many previous studies confirmed that using Mo-based catalysts increases the selectivity of phenol production in the HDO reaction of guaiacol. Although the overall HDO yield of guaiacol increased as the reaction temperature and hydrogen pressure increased, the selectivity of phenol was significantly dependent on the type and preparation method of the catalyst. In the available literature, the debate about the active phase of the catalyst is still inconclusive. Recently, Baddour et al. reported transition-metal-modified  $\beta$ -Mo<sub>2</sub>C catalysts to alter the catalytic function in the HDO of guaiacol [49]. The HDO and hydrogenation performance was enhanced by tuning the H-site and acid-site densities by adding other metals to  $\beta$ -Mo<sub>2</sub>C. To further improve the performance of the existing Mo<sub>2</sub>C catalyst, research is being actively conducted to develop a bifunctional catalyst by adding other metals [50–55].

Recently, metal-organic framework (MOF)-derived porous carbon catalysts have attracted attention as highly dispersed metal-supported carbon catalysts because of their high specific surface areas, tunable compositions, and well-defined porous structure [15,56–60]. Zeolitic imidazolate frameworks (ZIFs) are a unique subclass of MOFs that can be directly converted into nitrogen (N)-doped graphitic carbon frameworks with a uniform distribution of metal/metal oxides by a simple pyrolysis process [61–63]. In particular, doping nitrogen atoms into the carbon network after carbonization of ZIFs not only increases the dispersion of active metals (or oxides) on the carbon, but also activates the deposited species [62]. Nitrogen-doped carbon induces charge delocalization of C atoms near N atoms, resulting in a highly positive charge density that is favorable for the adsorption of compounds containing nitro groups. Yan et al. reported that Co nanoparticles produced by calcination of Zn/Co-ZIF-9 were activated by N-doped carbons, because nitrogen atoms can act as electron withdrawing groups that change the electron density of the metal centers [62]. The electron transfer from Co nanoparticles to N-doped carbon further enhanced the interaction between Co and carbon. Bimetals or multimetals derived from ZIFs can further improve catalytic performance than single metals [63]. Kui et al. reported that mixed metal Zn/Co-ZIFs had improved physical and chemical properties compared to single metal ZIFs [63]. They found that Zn/Co-ZIFs with a sodalite pore structure similar to ZIF-8 and ZIF-67 had better CO<sub>2</sub> conversion to cyclic carbonates as well as improved surface area and thermal stability compared to single-metal ZIFs (ZIF-8 and ZIF-67). ZIF-8 has a microporous structure and is easily transformed into carbon with a large surface area and uniformly distributed nitrogen after pyrolysis. However, ZIF-8 has disadvantages, such as a low degree of graphitization. Contrastingly, ZIF-67 exhibited a well-developed mesoporous structure but low nitrogen content and low specific surface area after carbonization. Thus, porous N-doped carbon catalysts derived from the combination of Zn-based ZIF-8 and Co-based ZIF-67 exhibit synergetic properties that combine the advantages of both ZIFs [64–67]. Hence, the resulting bimetallic ZIFs (BMZIFs) are expected to enhance the catalytic performance by utilizing two or more metal species that are highly dispersed in a well-defined carbon structure.

Inspired by the advantages of BMZIF, we designed BMZIF-decorated Mo carbide catalysts (Mo<sub>2</sub>C@BMZIF, MoO<sub>3</sub>@BMZIF) for the HDO of guaiacol to produce phenol at high conversion and selectivity. A uniform layer of BMZIF was controllably coated on the surface of MoO<sub>3</sub> nanorods. During controlled carbonization at different temperatures, the structure of BMZIFs was changed to metal oxide (ZnO and CoO) on highly dispersed N-doped carbons, while the MoO<sub>3</sub> nanorods were transformed into the Mo<sub>2</sub>C phase, creating a core@shell structure (Scheme 1b) [67]. By comparing the pristine and monometallic catalysts, the synergetic catalytic performance of Mo<sub>2</sub>C@BMZIF was demonstrated to produce phenol with high selectivity in the catalytic HDO of guaiacol.

## 2. Results and Discussion

### 2.1. Characterization of Catalysts

A BMZIF-based N-doped carbon composite was produced by the carbonization of BMZIF-coated  $\text{MoO}_3$  nanorods (Scheme 1b). Highly crystalline  $\text{MoO}_3$  nanorods with well-defined structures were synthesized via a simple hydrothermal method [68]. Field-emission scanning electron microscopy (FE-SEM) and transmission electron microscopy (TEM) images show a very smooth surface, and a rectangle-like cross-section of the as-prepared  $\text{MoO}_3$  nanorods with an average width of ca. 250 nm (Figure 1a,d). Then, the synthesized  $\text{MoO}_3$  nanorods were decorated with ZIF to produce an  $\text{MoO}_3$ @ZIF core@shell structure. When two metal nitrate salts (20 molar ratio of  $\text{Zn}^{2+}/\text{Co}^{2+}$ ) and 2-methylimidazole as an organic linker were mixed with  $\text{MoO}_3$  nanorods in the presence of polyvinylpyrrolidone (PVP), a  $\text{MoO}_3$ @BMZIF core@shell structure was generated [67]. As shown in Figure 1b,e, FE-SEM and TEM images confirm the core@shell structure of the  $\text{MoO}_3$ @BMZIF with a porous shell on the surface of the  $\text{MoO}_3$  nanorod. By carbonization at high temperatures (700–800 °C) under an  $\text{N}_2$  atmosphere, the core  $\text{MoO}_3$  nanorods were converted to  $\text{Mo}_2\text{C}$ . In contrast, the ZIF shell was transformed into a porous N-doped carbon with highly dispersed  $\text{ZnO}$  and  $\text{CoO}$  particles. Figure 1c,f show that the distinct core@shell structure of the original  $\text{MoO}_3$ @BMZIF was preserved even after high-temperature calcination at 700 °C for 4 h (denoted as  $\text{Mo}_2\text{C}$ @BMZIF-700 °C (4 h)). In addition, it was confirmed that the rough, porous shell was transformed into a softer, curved surface through the carbonization process.

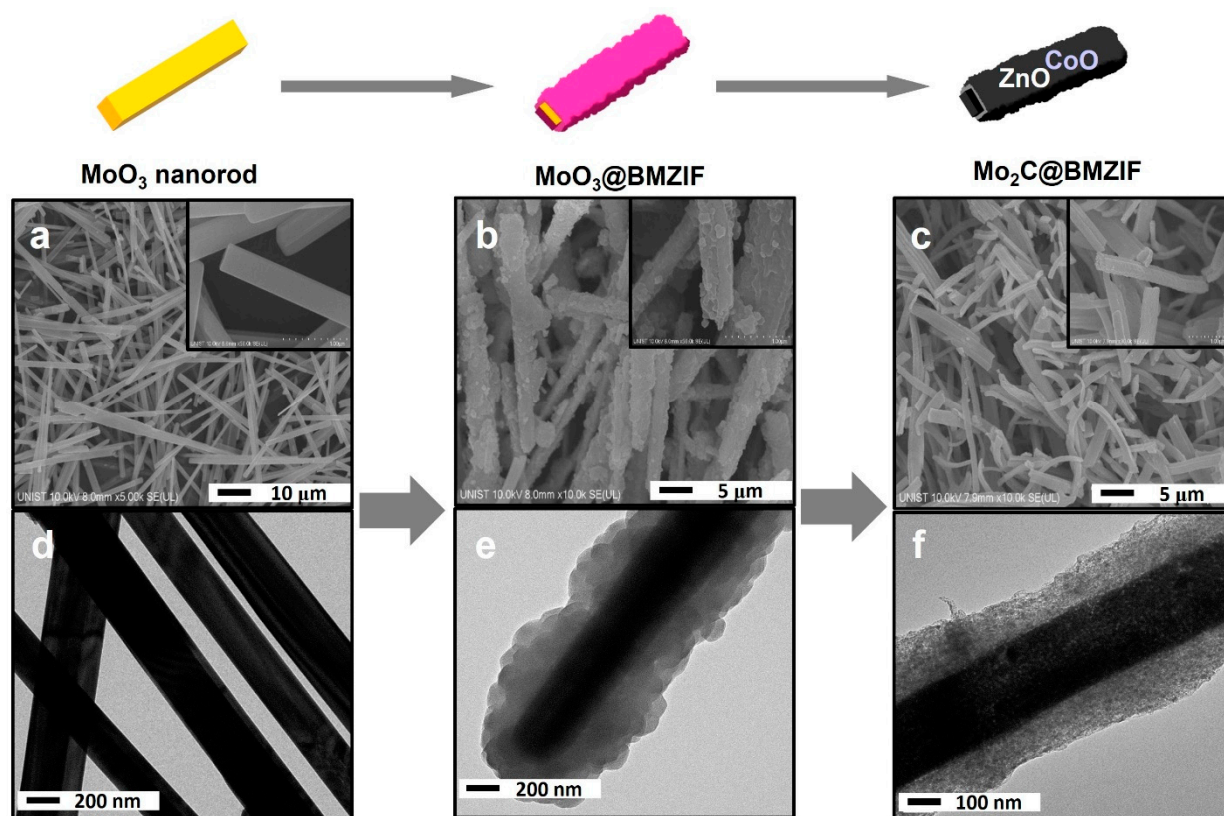


**Figure 1.** Structural change in ZIF-decorated Mo carbide nanorods. (a–c) FE-SEM and (d–f) TEM images of (a,d) as-prepared  $\text{MoO}_3$  nanorods, (b,e)  $\text{MoO}_3$ @BMZIF composite, and (c,f)  $\text{Mo}_2\text{C}$ @BMZIF-700 °C (4 h) core@shell structure after carbonization under an  $\text{N}_2$  atmosphere at 700 °C for 4 h.

X-ray diffraction (XRD) analysis was used to confirm the structural evolution of  $\text{MoO}_3$ @BMZIF to  $\text{Mo}_2\text{C}$ @BMZIF. As-synthesized  $\text{MoO}_3$  nanorods showed a typical XRD pattern of  $\text{MoO}_3$  (JCPDS No. 89–5108) with high intensity, confirming the successful

formation of the crystalline  $\text{MoO}_3$  phase (Figures 2a and S1). When metal precursors containing Zn and Co were mixed with  $\text{MoO}_3$  nanorods in the presence of 2-methylimidazole, BMZIF shells were formed around the  $\text{MoO}_3$  surface. During carbonization at  $700^\circ\text{C}$ , an ordered ZIF structure was formed and attached to the  $\text{MoO}_3$  surface. Depending on the carbonization time at  $700^\circ\text{C}$ , the structural transformations in the core@shell composite were identified using XRD and TEM analyses. The XRD peaks in the range of  $5\text{--}40^\circ$  sharpened as the carbonization time of  $\text{MoO}_3\text{@BMZIF}$  increased from 0.25 to 1 h, indicating that a well-defined ZIF structure was formed (Figure 2a). When the reaction time was increased beyond 5 h, the TEM results showed an overgrowth of BMZIF on the surface of the  $\text{MoO}_3$  nanorods. The well-covered BMZIF shells were detached from the  $\text{MoO}_3$  surface and collapsed to form aggregated clusters (Figure S2a–c). After carbonization at  $700^\circ\text{C}$  for 4 h under  $\text{N}_2$  atmosphere, the produced  $\text{Mo}_2\text{C@BMZIF-}700^\circ\text{C}$  (4 h) showed a distinct XRD peak at  $34.5^\circ$ ,  $39.5^\circ$ , and  $52.2^\circ$ . These peaks correspond to the (002), (211), and (221) planes of orthorhombic  $\text{Mo}_2\text{C}$  (JCPDS no. 77–0720) by eliminating the original  $\text{MoO}_3$  peaks (Figure 2b) [67]. In addition, the BMZIF shell was transformed into oxide species, such as ZnO and CoO, while the organic framework of the ZIF was converted into an N-doped carbon structure (Table S1). In addition to the  $\text{Mo}_2\text{C}$  peaks, the XRD patterns also detected diffractions for metal oxides as active sites, such as ZnO and CoO, which were derived from the BMZIF.

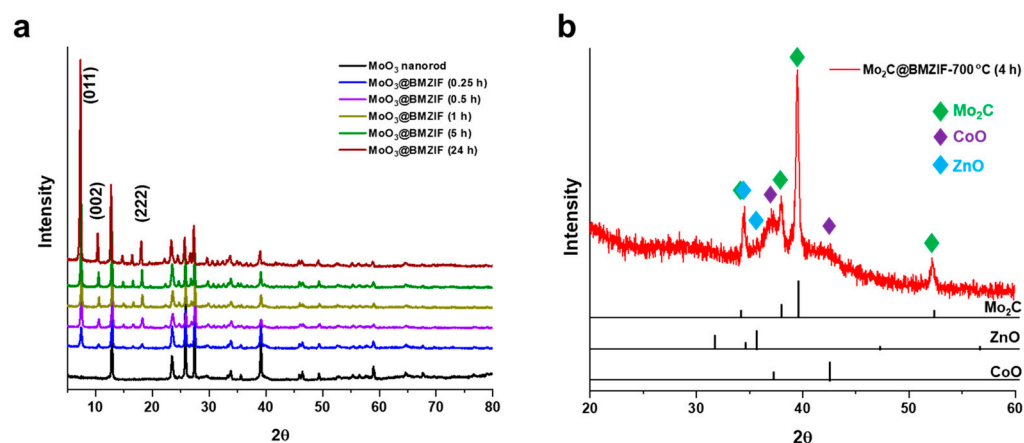


**Figure 2.** XRD patterns of (a) as-prepared  $\text{MoO}_3$  nanorods and  $\text{MoO}_3\text{@BMZIF}$  catalysts obtained at different reaction times (0.25–24 h), and (b)  $\text{Mo}_2\text{C@BMZIF-}700^\circ\text{C}$  (4 h).

Along with TEM and XRD analyses, the energy-dispersive X-ray spectroscopy (EDS) elemental mapping results further demonstrated the well-defined core@shell structure of  $\text{Mo}_2\text{C@BMZIF}$  with ZnO and CoO species dispersed in N-doped carbon and the transformed  $\text{Mo}_2\text{C}$  nanorod core. Before carbonization, the pristine  $\text{MoO}_3\text{@BMZIF}$  nanorods showed a well-defined core@shell structure with an outer ZIF shell containing a homogeneous distribution of Co and Zn species, as well as the  $\text{MoO}_3$  core (Figure S3). During carbonization, the internal  $\text{MoO}_3$  nanorods were reduced to form  $\text{MoO}_2$  in the presence of carbon in the following fashion (Equation (1)) [67]:



As the reaction proceeded,  $\text{MoO}_2$  was further carbonized to create  $\text{Mo}_2\text{C}$  (Equation (2)) [67]:



Tian et al. reported a similar structural evolution of  $\text{MoO}_3\text{@BMZIF}$  to  $\text{Mo}_2\text{C@BMZIF}$  nanorods by carbonization [67]. The HR-TEM image of  $\text{Mo}_2\text{C@BMZIF-}700^\circ\text{C}$  (4 h) shows lattice fringes of  $\text{Mo}_2\text{C}$  with a lattice space of 0.22 nm, which is assigned to the (211) plane of orthorhombic  $\text{Mo}_2\text{C}$  (Figure 3a). Figure 3b–d further demonstrate that the BMZIF

shell generates ZnO and CoO nanoparticles with a lattice space of 0.33 nm and 0.25 nm, corresponding to the (002) and (111) planes, respectively [67]. The EDS mapping results show the core@shell structure of Mo<sub>2</sub>C@BMZIF-700 °C (4 h) with a uniform elemental distribution of Zn, Co, N, O, and C, which originated from the BMZIF shell coated on the core MoO<sub>3</sub> (Figure 3e). It was also confirmed that the core@shell structure of Mo<sub>2</sub>C@BMZIF-700 °C (4 h) was maintained after carbonization at 700 °C for 4 h. The ZIF shell produced bimetallic elements of both ZnO and CoO, homogeneously dispersed in N-doped carbon. The change in porosity during carbonization was confirmed by N<sub>2</sub> adsorption–desorption isotherms of MoO<sub>3</sub>@BMZIF before and after carbonization (Figure S4). The as-prepared MoO<sub>3</sub>@BMZIF exhibits a higher Brunauer–Emmett–Teller (BET) surface area of 1033 m<sup>2</sup> g<sup>−1</sup> and a total pore volume of 0.48 cm<sup>3</sup> g<sup>−1</sup> estimated at p/p<sup>0</sup> = 0.99 (Figure S4a). In contrast, the N<sub>2</sub> adsorption–desorption isotherm of Mo<sub>2</sub>C@BMZIF-700 °C (4 h) shows a type-IV hysteresis loop, revealing its mesoporous nature (Figure S4b). The measured BET surface area of Mo<sub>2</sub>C@BMZIF-700 °C (4 h) is 107 m<sup>2</sup> g<sup>−1</sup>, a considerably decreased value compared to MoO<sub>3</sub>@BMZIF without carbonization. This indicates that the BMZIF has a reduced surface area due to shrinkage during carbonization at 700 °C; however, its porous nature is still maintained.

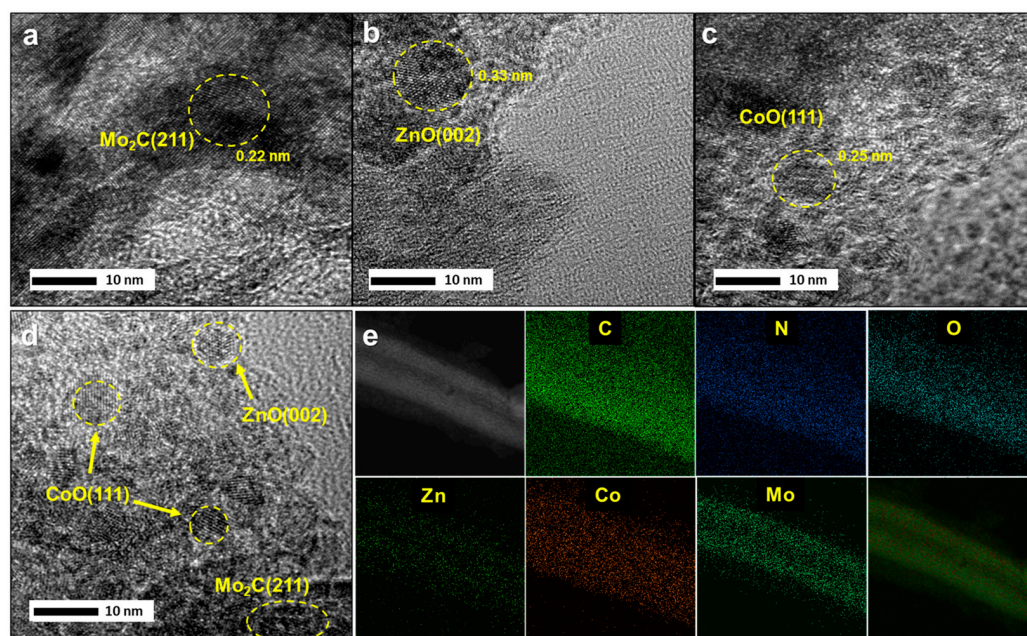


**Figure 3.** (a–d) HR-TEM images of Mo<sub>2</sub>C@BMZIF-700 °C (4 h) showing Mo<sub>2</sub>C, ZnO, and CoO phases and (e) corresponding elemental EDS maps of Mo<sub>2</sub>C@BMZIF-700 °C (4 h).

X-ray photoelectron spectroscopy (XPS) was performed to investigate the active species and their surface states. The main XPS spectrum of Mo<sub>2</sub>C@BMZIF-700 °C (4 h) verifies the presence of Mo, C, N, O, Zn, and Co elements (Figure 4a). To compare the Mo 3d spectrum of Mo<sub>2</sub>C@BMZIF-700 °C (4 h), pure Mo<sub>2</sub>C nanorods were prepared by carbonization at 700 °C for 4 h without adding ZIF. The Mo 3d spectra are split into 3d<sub>5/2</sub> and 3d<sub>3/2</sub> peaks because of the spin-orbital coupling effect (Figure 4b) [69,70]. For the converted Mo<sub>2</sub>C@BMZIF-700 °C (4 h), the shoulder of Mo 3d<sub>5/2</sub> with a binding energy of 228.6 ± 0.1 eV can be attributed to Mo<sup>2+</sup> species, which do not appear in MoO<sub>3</sub> nanorods. On the other hand, the Mo 3d<sub>5/2</sub> peak at 229.8 eV ± 0.1 eV is characteristic of Mo<sup>4+</sup>, indicating that the surface of Mo<sub>2</sub>C@BMZIF-700 °C (4 h) is highly oxidized to have both Mo<sup>4+</sup> and Mo<sup>2+</sup> species [67,71–73]. It is worth noting that the Mo<sup>2+</sup> 3d<sub>5/2</sub> (228.6 ± 0.1 eV) and Mo<sup>4+</sup> 3d<sub>5/2</sub> (229.8 ± 0.1 eV) peaks of Mo<sub>2</sub>C@BMZIF-700 °C (4 h) shift to lower binding energies compared to those of the bare Mo<sub>2</sub>C nanorod (Figure 4b) [72]. This result demonstrated an interaction between the metal atoms from the shell (ZnO and CoO) and the Mo atoms

of the core nanorod. The deconvoluted Mo 3d peak reveals two oxidation states of Mo ( $\text{Mo}^{2+}$  and  $\text{Mo}^{4+}$ ) on the surface of  $\text{Mo}_2\text{C}@BMZIF-700\text{ }^\circ\text{C}$  (4 h) (Figure 4c) [73]. Although the original  $\text{MoO}_3$  nanorods display only  $\text{Mo}^{4+}$ , characteristic XPS peaks corresponding to  $\text{Mo}^{2+}$  appear only in the converted  $\text{Mo}_2\text{C}$  nanorods [67]. In addition, the Zn  $2p_{3/2}$  peak of the  $\text{Mo}_2\text{C}@BMZIF-700\text{ }^\circ\text{C}$  (4 h) with a binding energy of 1021.81 eV shows a shift to higher binding energy compared to pure ZnO(II) (1021 eV) (Figure S5a). Similarly, the Co  $2p_{3/2}$  peak with a binding energy of 781.57 eV shows a shift to a higher binding energy compared to pure CoO (780 eV) (Figure S5b). These results further demonstrate the interaction between the metals in the shell (ZnO and CoO) and Mo atoms in the core nanorods. The presence of nitrogen in the  $\text{Mo}_2\text{C}@BMZIF-700\text{ }^\circ\text{C}$  (4 h) is caused by the pyrolysis of the 2-methylimidazole organic linker. Essentially, the methylimidazole organic linker plays a vital role in generating N-doped carbon and homogeneously dispersing ZnO and CoO nanoparticles on the  $\text{Mo}_2\text{C}@BMZIF-700\text{ }^\circ\text{C}$  (4 h). Figure 4d shows the N 1s spectrum fitted into three peaks, corresponding to pyridinic nitrogen (398.6 eV), pyrrolic nitrogen (399.1 eV), and graphitic nitrogen (400.9 eV), revealing the production of N-doped carbons [73–75].

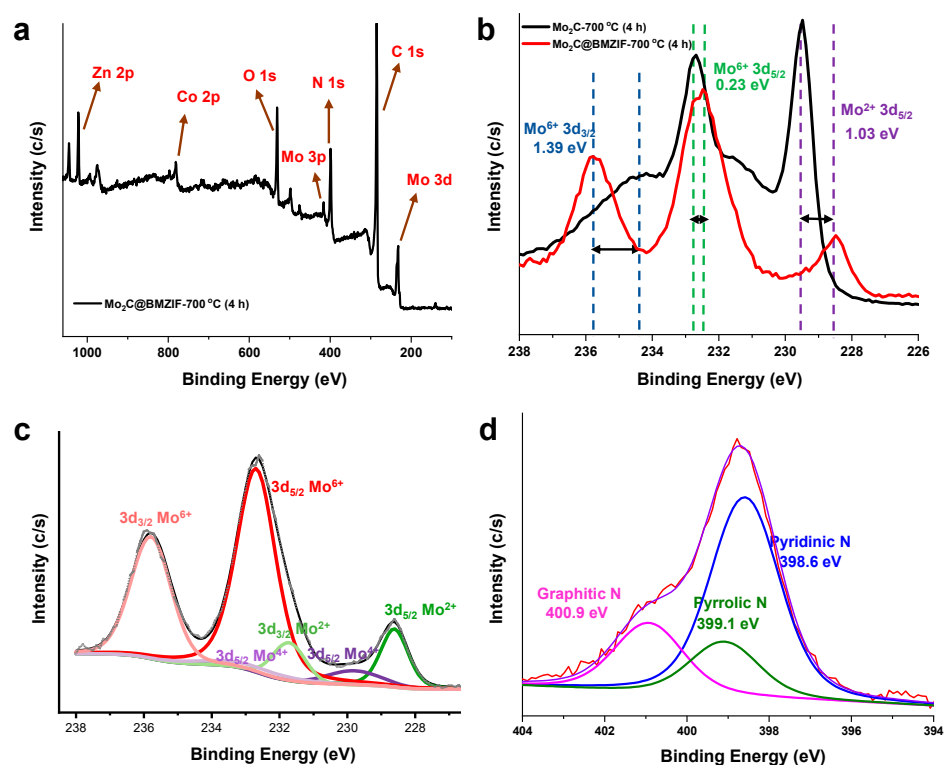


**Figure 4.** (a) XPS profiles of  $\text{Mo}_2\text{C}@BMZIF-700\text{ }^\circ\text{C}$  (4 h). (b) XPS Mo 3d spectra compared to a pure  $\text{Mo}_2\text{C}-700\text{ }^\circ\text{C}$  (4 h) nanorod and the  $\text{Mo}_2\text{C}@BMZIF-700\text{ }^\circ\text{C}$  (4 h) core@shell structure. XPS (c) Mo 3d and (d) N 1s spectra of  $\text{Mo}_2\text{C}@BMZIF-700\text{ }^\circ\text{C}$  (4 h).

## 2.2. Hydrodeoxygenation of Guaiacol over $\text{Mo}_2\text{C}@BMZIF$ Catalysts

The catalytic HDO reaction of guaiacol was performed under optimized reaction conditions (330  $^\circ\text{C}$ , 4 MPa of  $\text{H}_2$  for 4 h). Different  $\text{Mo}_2\text{C}@BMZIF$  catalysts produced at different carbonization temperatures and times were used. The uncatalyzed HDO reaction exhibited a very low guaiacol conversion. Figure 5a shows the guaiacol conversion, selectivity, and product distributions over  $\text{Mo}_2\text{C}@BMZIF-700\text{ }^\circ\text{C}$  (2 h),  $\text{Mo}_2\text{C}@BMZIF-700\text{ }^\circ\text{C}$  (4 h), and  $\text{Mo}_2\text{C}@BMZIF-800\text{ }^\circ\text{C}$  (2 h). For all the tested catalyzed reactions, phenol was the main product produced from guaiacol. Among the catalysts,  $\text{Mo}_2\text{C}@BMZIF-700\text{ }^\circ\text{C}$  (4 h) showed the best conversion of guaiacol (97%) and the highest phenol selectivity (70%).  $\text{Mo}_2\text{C}@BMZIF-700\text{ }^\circ\text{C}$  (2 h) and  $\text{Mo}_2\text{C}@BMZIF-800\text{ }^\circ\text{C}$  (2 h) catalysts showed 82% and 83% conversion, respectively. The guaiacol conversion and phenol selectivity proved to be

highly affected by the distribution of active species ( $\text{MoO}_3$ ,  $\text{Mo}_2\text{C}$ ,  $\text{ZnO}$ , and  $\text{CoO}$ ), which were generated by different carbonization processes at different temperatures and times. The role of each active species is discussed in the next section. The most effective and active catalyst for the HDO of guaiacol was  $\text{Mo}_2\text{C}@BMZIF-700\text{ }^\circ\text{C}$  (4 h). The least active catalyst had not only a lower guaiacol conversion but also a lower selectivity for phenol, causing the reaction to produce more anisole and cyclohexene as by-products.

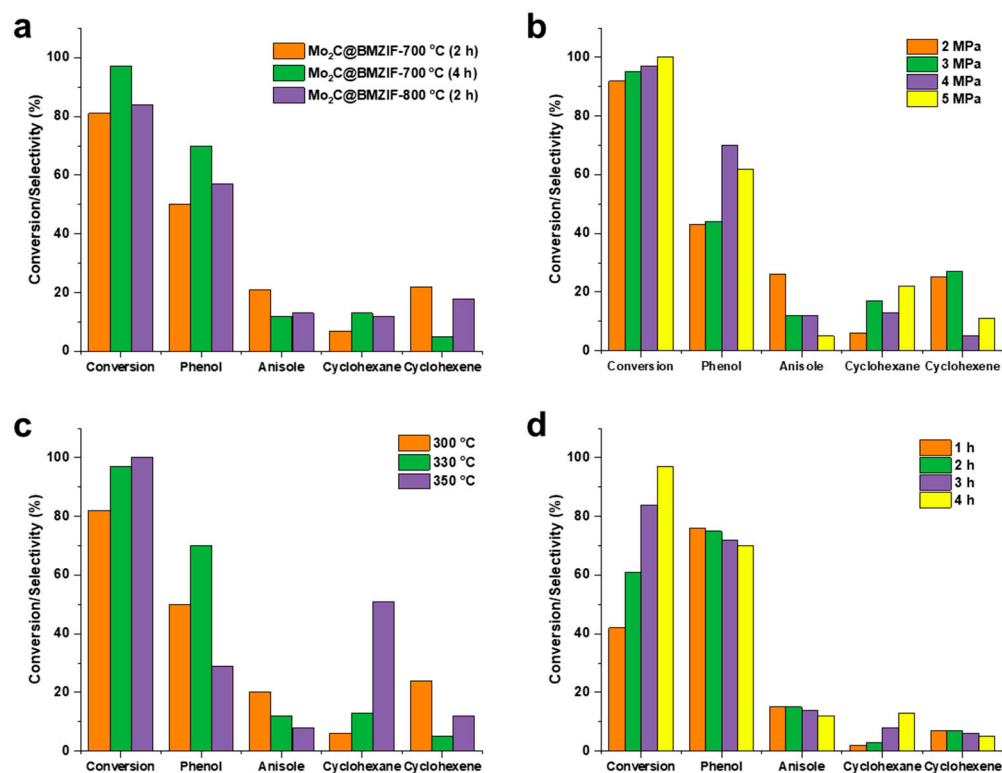


**Figure 5.** Conversion and product selectivity of catalytic HDO of guaiacol over  $\text{Mo}_2\text{C}@BMZIF$  catalysts as a function of (a) carbonization condition of the catalyst, (b) reaction pressure, (c) temperature, and (d) time (a standard reaction condition: catalyst 60 mg, guaiacol 0.12 g, *n*-decane 20 mL, 330 °C, 4 h, 4 MPa).  $\text{Mo}_2\text{C}@BMZIF-700\text{ }^\circ\text{C}$  (4 h) catalyst was used for (b–d).

The effects of  $\text{H}_2$  pressure (2–5 MPa), reaction temperature (300–350 °C), and time (1–4 h) were investigated over  $\text{Mo}_2\text{C}@BMZIF-700\text{ }^\circ\text{C}$  (4 h) since it was the most effective catalyst (Figure 5a). Figure 5b shows that the guaiacol conversion and phenol selectivity increased linearly as the  $\text{H}_2$  pressure was increased from 2 to 5 MPa at 330 °C. The highest phenol conversion (97%) and selectivity (70%) were obtained under 4 MPa of  $\text{H}_2$  pressure. Furthermore, increasing the  $\text{H}_2$  pressure to 5 MPa converted 100% of the guaiacol but had lower selectivity to phenol (62%).

As expected, the overall conversion increased linearly with the reaction temperature under the optimum  $\text{H}_2$  pressure of 4 MPa and reaction time of 4 h (Figure 5c). The phenol selectivity increased from 50% to 70% as the reaction temperature increased from 300 to 330 °C. A further increase in the reaction temperature to 350 °C resulted in the complete conversion of guaiacol. However, the selectivity towards phenol decreased substantially because further hydrogenation occurred, thus, producing cyclohexane at the expense of phenol. Therefore, continuously increasing the reaction temperature above 350 °C is not recommended for the  $\text{Mo}_2\text{C}@BMZIF-700\text{ }^\circ\text{C}$  (4 h) catalyzed HDO reaction because it promotes the hydrogenation of the aromatic ring and reduces the selectivity of phenol [76,77].

The influence of reaction time was investigated at a reaction temperature of 330 °C and an  $\text{H}_2$  pressure of 4 MPa, since these were the optimum reaction conditions. An increase in the guaiacol conversion was observed upon increasing the reaction time (Figure 5d).



When the reaction was run for 1 h, a lower guaiacol conversion (43%) was obtained, while phenol selectivity was 76%. However, when the reaction time was increased to 4 h, the reaction showed the highest guaiacol conversion of 97%, and the phenol selectivity was reduced to 70%. It was deduced that the hydrogenation reaction conversion increased with increased reaction time but slightly decreased the phenol selectivity due to the formation of cyclohexane. These outcomes were also consistent with the findings of various researchers [78,79].

To understand the role of each active species, we prepared various supported catalysts and monometallic catalysts with and without Mo-based nanorods. When Mo-based nanorods were solely used without ZIF coating, the guaiacol conversion of MoO<sub>3</sub> and Mo<sub>2</sub>C-700 °C (4 h) was 55% and 38%, respectively (Figure 6). Although MoO<sub>3</sub> shows higher conversion than Mo<sub>2</sub>C in the present condition, both catalysts showed high catalytic selectivity toward phenol (>60%), demonstrating that Mo-based catalysts are suitable for high phenol production [18,80–85]. Both phases can further enhance guaiacol conversion by depositing additional metal species. When a Co or Zn precursor was impregnated on the Mo<sub>2</sub>C nanorods, which were carbonized at 700 °C for 4 h under an N<sub>2</sub> atmosphere, the resulting Mo<sub>2</sub>C/Co-700 °C (4 h) and Mo<sub>2</sub>C/Zn-700 °C (4 h) showed higher conversion of guaiacol than the Mo<sub>2</sub>C-700 °C (4 h) nanorod (Figure 6). When two single metallic catalysts were physically mixed (Mo<sub>2</sub>C/Co+Zn-700 °C (4 h)) to be used for the HDO reaction, the conversion of guaiacol (70%) was higher than that of the individual catalysts. However, when two metallic precursors were formed as a BMZIF shell, the Mo<sub>2</sub>C@BMZIF-700 °C (4 h) catalyst exhibited the best performance. This outcome may be due to the uniform distribution of Co and Zn metals over the entire N-doped carbon network (Figure 6). Therefore, it was concluded that the enhanced catalytic performance of the Mo<sub>2</sub>C@BMZIF-700 °C (4 h) catalyst in the HDO of guaiacol for the selective production of phenol resulted from the synergistic effect of well-defined ZnO and CoO species dispersed in porous N-doped carbon and the core Mo<sub>2</sub>C nanorod. The ZnO and CoO species produced by the BMZIF shell were in intimate contact with the Mo<sub>2</sub>C surface. When Mo, Co, and Zn oxides were deposited on AC by impregnation, the resulting Mo+Co+Zn/AC catalyst showed an 82% guaiacol conversion while the phenol selectivity was 58% (Figure 6). Likewise, the AC-supported single metal oxide catalysts (Zn/AC and Co/AC) exhibited poor conversion (32% for Zn/AC and 28% for Co/AC) and phenol selectivity of less than 40%. From these results, it can be deduced that the well-defined Mo<sub>2</sub>C@BMZIF-700 °C (4 h) has distinct structural and catalytic properties. The BMZIF shells provide carbon matrices with nitrogen originating from the pyrolysis of organic linkers. The N-doped carbon anchors ZnO and CoO species to guarantee high dispersion in the porous carbon structure. It has been reported that graphitic nitrogen can donate extra free electrons to anchor active metal species, and pyrrolic and pyridinic nitrogen also provide more active sites [68]. The highly dispersed and stable ZnO and CoO species on porous N-doped carbon provide additional activity to the Mo<sub>2</sub>C nanorods. When the metals are supported on the surface of the Mo<sub>2</sub>C nanorods, the Zn and Co species are easily aggregated because the low surface area of Mo<sub>2</sub>C nanorods cannot effectively and stably disperse the metal. The TEM image of the impregnated Mo<sub>2</sub>C/Zn+Co-700 °C (4 h) catalyst shows aggregated metal species, which may have caused a decrease in catalytic activity (Figure S6a). Furthermore, the synergistic structural and catalytic effects of Zn, Co, and Mo species in the AC-supported catalyst Mo+Co+Zn/AC were not observed (Figure S6b).

The synergistic effect of the Mo<sub>2</sub>C@BMZIF-700 °C (4 h) catalyst derived from well-defined ZnO and CoO species dispersed in porous N-doped carbon in intimate contact with the core Mo<sub>2</sub>C nanorod was further confirmed by XPS results. In Figure 4b, the binding energies of the Mo<sup>2+</sup> 3d<sub>5/2</sub> and Mo<sup>4+</sup> 3d<sub>5/2</sub> peaks of Mo<sub>2</sub>C@BMZIF-700 °C (4 h) shifted to a lower binding energy as compared to the pristine Mo<sub>2</sub>C nanorod. The shift in the binding energy of the Mo spectra at Mo<sub>2</sub>C@BMZIF-700 °C (4 h) indicates a change in the electronic structure of Mo [86]. Tran et al. [87] reported that the shift in the binding energies of W and Mo in the MoWC catalyst could be attributed to the change in the electron density of W

and Mo atoms. The chemical shift shown in XPS originates from the change in electron density due to the interaction between Mo and W atoms, enabling electron transfer from W to Mo. Liu et al. [88] reported that the valence distribution of Mo in the 20Cu20Mo<sub>2</sub>C/M41 catalyst was affected by the presence of Cu atoms. The XPS deconvolution results for Mo confirmed four molybdenum species in the 20Cu20Mo<sub>2</sub>C/M41 catalyst. From these results, it is speculated that the shift in the binding energy in the XPS profile is due to the charge transfer between the Mo atom of the core and the Zn and Co atoms of the shell consisting of N-doped carbon [86,89,90]. The collective interaction of well-dispersed Mo, Co, and Zn metal atoms, as well as the N atom in the porous carbon, synergistically promotes high phenol selectivity in the HDO of guaiacol, which was not achieved by other supported catalysts. The well-defined core@shell structure consisting of Mo<sub>2</sub>C@BMZIF nanorods with ZnO and CoO species dispersed in the N-doped porous carbon shell and the Mo<sub>2</sub>C nanorod core satisfied all these requirements to improve the guaiacol conversion and phenol selectivity.

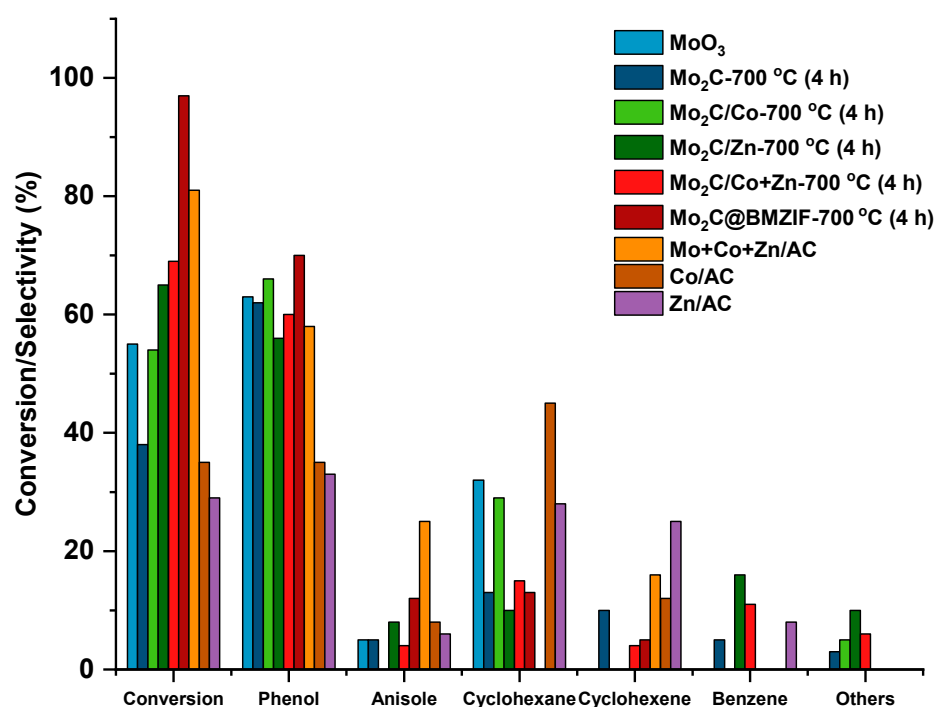


**Figure 6.** Comparison of conversion and product selectivity of catalytic HDO of guaiacol over various catalysts (reaction condition: catalyst 60 mg, guaiacol 0.12 g, *n*-decane 20 mL, 330 °C, 4 h, 4 MPa).

To evaluate whether the Mo<sub>2</sub>C@BMZIF-700 °C (4 h) catalyst can be applied to the HDO reaction of various lignin derivatives other than guaiacol, we performed a catalytic HDO reaction using syringol and vanillin (Table S2) [85]. The HDO reaction using syringol showed an 82% conversion under the optimized reaction conditions (i.e., 330 °C and 4 MPa of H<sub>2</sub> for 4 h). Syringol with two methoxy groups was deoxygenated into guaiacol and phenol, depending on the number of methoxy groups lost by H<sub>2</sub>. Although the HDO selectivity varied with reaction times, guaiacol and phenol were still the significant products, demonstrating the high HDO selectivity of the Mo<sub>2</sub>C@BMZIF-700 °C (4 h) catalyst (Table S2) [85]. For example, the guaiacol selectivity decreased from 36 to 12%, while that of phenol increased from 18 to 46% with an increase in reaction time (2–4 h). This result was attributed to the conversion of guaiacol to phenol, which improved the overall conversion from 60 to 82% due to the loss of two methoxy groups by the full HDO. When vanillin was used as a substrate for HDO, a 100% conversion was achieved with 79% toluene selectivity due to the selective HDO reaction by the Mo<sub>2</sub>C@BMZIF-700 °C (4 h) catalyst.

The experiments confirmed that a well-designed Mo<sub>2</sub>C@BMZIF catalyst could be applied to the HDO reaction of various lignin derivatives.

The recyclability of the Mo<sub>2</sub>C@BMZIF-700 °C (4 h) catalyst was tested by three consecutive cycles of the guaiacol HDO reaction in 4 MPa of H<sub>2</sub> at 330 °C for 4 h. There was no apparent loss of guaiacol conversion, even after three cycles (Figure 7a). In XRD, the spent Mo<sub>2</sub>C@BMZIF-700 °C (4 h) catalyst showed no change in the crystalline structure after three catalytic cycles (Figure 7b). In addition, the original morphology was preserved, as confirmed by FE-SEM and TEM images (Figure 7c,d), demonstrating the reusability and recyclability of the Mo<sub>2</sub>C@BMZIF catalyst without changing its structure or active species.

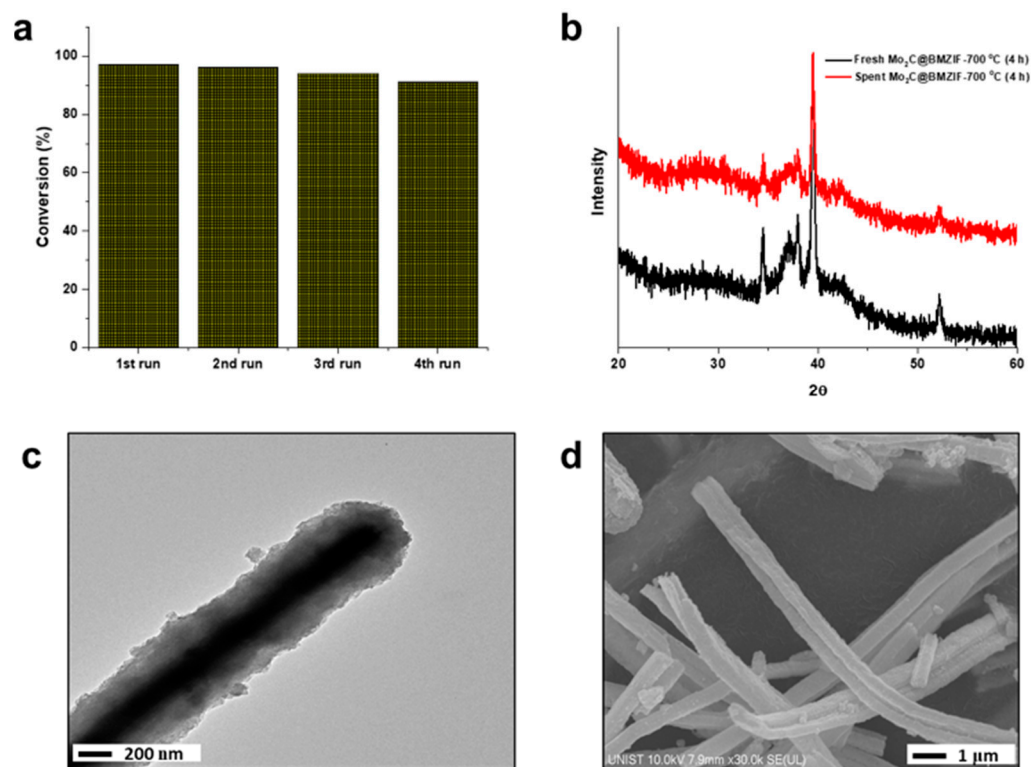


**Figure 7.** (a) Catalytic recyclability test for 4 runs (catalyst 60 mg, guaiacol 0.12 g, *n*-decane 20 mL, 330 °C, 4 h, 4 MPa), (b) XRD, (c) TEM, and (d) FE-SEM results of the spent Mo<sub>2</sub>C@BMZIF-700 °C (4 h) catalyst after 4 runs.

### 3. Materials and Methods

#### 3.1. Chemicals

Ethanol (anhydrous 99.9%) and HNO<sub>3</sub> (60%) were purchased from Samchun Chemicals. Ammonium heptamolybdate tetrahydrate ((NH<sub>4</sub>)<sub>6</sub>Mo<sub>7</sub>O<sub>24</sub>·4H<sub>2</sub>O), polyvinylpyrrolidone (300 K), Zn(NO<sub>3</sub>)<sub>2</sub>·6H<sub>2</sub>O, Co(NO<sub>3</sub>)<sub>2</sub>·6H<sub>2</sub>O, 2-methylimidazole, methanol (99.8%), and guaiacol (99%) were purchased from Sigma Aldrich.

#### 3.2. Preparation of MoO<sub>3</sub> Nanorods

MoO<sub>3</sub> nanorods were synthesized by following a previously reported hydrothermal reaction [71]. Briefly, 1.4 g of ammonium heptamolybdate tetrahydrate was dissolved in a mixture of 33 mL of 60% HNO<sub>3</sub> and 7 mL of deionized water. The solution was then heated at 200 °C for 20 h in a Teflon-lined stainless steel autoclave. The obtained product was washed with ethanol 2–3 times and dried at 80 °C overnight.

#### 3.3. Preparation of Composites and core@Shell Nanorods

MoO<sub>3</sub>@BMZIF and Mo<sub>2</sub>C@BMZIF were prepared according to a previously reported method with slight modifications [70]. To decorate BMZIF shells on the surface of MoO<sub>3</sub>,

0.15 g of synthesized MoO<sub>3</sub> nanorods (Section 2.1) were dispersed into 30 mL of methanol containing 0.5 g of polyvinylpyrrolidone (300 K). After vigorous stirring for 30 min, 15 mL of methanol solution containing 1.06 g of Zn(NO<sub>3</sub>)<sub>2</sub>·6H<sub>2</sub>O and 0.052 g of Co(NO<sub>3</sub>)<sub>2</sub>·6H<sub>2</sub>O were slowly added to the mixed solution and stirred for 2 h. Then, 2.5 g of 2-methylimidazole dissolved in 45 mL of methanol was slowly added to the above solution, followed by vigorous stirring for 30 min. The final product of MoO<sub>3</sub>@BMZIF was collected by centrifugation, washed with methanol 2–3 times, and dried at 60 °C overnight. The as-prepared MoO<sub>3</sub>@BMZIF was carbonized at 700–800 °C under N<sub>2</sub> atmosphere for 2–4 h at a heating rate of 5 °C min<sup>-1</sup> to obtain Mo<sub>2</sub>C@BMZIF core@shell nanorods.

### 3.4. Preparation of Reference Catalysts

To identify the active sites of the Mo<sub>2</sub>C@BMZIF core@shell nanorods, various reference catalysts were prepared with and without Mo-based nanorods, as well as monometallic-supported catalysts. To prepare monometallic ZIF-coated Mo<sub>2</sub>C nanorods, the as-synthesized MoO<sub>3</sub> was slowly added to the Zn or Co precursor solution (the required number of metals in 5 mL of deionized water) in a similar manner to MoO<sub>3</sub>@BMZIF. After stirring at 25 °C for 2 h, 2-methylimidazole in methanol was added, then the solid product was separated and dried at 80 °C. Carbonization was then carried out to generate monometallic species, such as ZnO or CoO dispersed in N-doped carbon at 500 °C for 2 h under N<sub>2</sub> flow. The obtained catalyst was further calcined at 700 °C for 4 h under 5% H<sub>2</sub> to produce Mo<sub>2</sub>C@Zn-700 °C (4 h) and Mo<sub>2</sub>C@Co-700 °C (4 h). AC-supported catalysts were prepared using the impregnation method. Briefly, 1 g of AC (Vulcan XC 72R) was slowly added to the metal precursor solution (the required amount of Zn(NO<sub>3</sub>)<sub>2</sub>·6H<sub>2</sub>O (0.069 g) and/or Co(NO<sub>3</sub>)<sub>2</sub>·6H<sub>2</sub>O (0.091 g) in 5 mL of deionized water). After stirring at 25 °C for 2 h and drying at 80 °C for 4–6 h, calcination was carried out to impregnate the metal on AC at 500 °C for 2 h under N<sub>2</sub> flow. The obtained catalyst was further calcined at 700 °C for 4 h under 5% H<sub>2</sub> to produce the Zn/AC and Co/AC catalysts. When three precursors were added to AC, the Mo+Co+Zn/AC mixture catalyst was produced using the same method. The bimetallic-supported catalyst, Mo<sub>2</sub>C@Zn+Co-700 °C (4 h), was prepared by using the calcined Mo<sub>2</sub>C nanorods at 700 °C for 4 h by impregnating Zn and Co precursors. The total loading of Zn+Co to the Mo<sub>2</sub>C was 3.2 wt %.

### 3.5. Catalyst Characterization

The structural characterization of the prepared catalysts was performed using FE-SEM (Hitachi S-4800 microscope) and TEM (JEOL, JEM-2100F) with EDS (Oxford instrument, X-Max 80T), N<sub>2</sub> physisorption by the BET (BELSorp-max) method, and powder XRD (PANalytical X'Pert Pro) using a Cu K $\alpha$  radiation source ( $\lambda = 0.154056$  nm). The surface chemical properties were characterized using the XPS (Thermo Fisher system) equipped with an Al K $\alpha$  radiation source. The composition of metals in the catalyst was determined by inductively coupled plasma–optical emission spectrometry (ICP–OES, Varian, 700-ES). The concentration of Co (or Cu) was calibrated using a multistandard solution (inorganic ventures). The digestion of the catalyst was carried out by dissolving the catalyst in aqua regia for 3 days. The solution was diluted with DI water and filtered to remove the carbon support before measurement.

### 3.6. Reaction Procedure and Product Analysis

For the standard HDO reaction of guaiacol, 0.12 g of guaiacol was dispersed in 20 mL of *n*-decane, and 0.06 g of the catalyst was added to the mixture. This mixture was added to an autoclave reactor with a 100-mL inner volume. After purging the reactor with H<sub>2</sub> gas, 4 MPa of H<sub>2</sub> was added to the reactor. The reactor was heated to 330 °C; aliquots were collected from the solution every 2 h. For the controlled tests, the reaction temperature, H<sub>2</sub> pressure, and reaction time varied from 300 to 350 °C, 2–5 MPa, and 1–4 h, respectively. After removing the solid from the mixture, the substrate conversion and product selectivity were quantified using GC FID. For the recycling test, the HDO reaction of guaiacol was

carried out at the same initial condition. After each reaction, the catalyst was separated by filtration from the reaction mixture, washed with ethanol, and dried in the air at 100 °C for 2 h. Then the recovered catalyst was used for the next run. The mass balance of the catalytic result was approximately 94%, which was determined by comparing the conversion calculated from guaiacol loss to the products produced [91]. Carbon balance was calculated by  $\Sigma (\text{carbon number} \times n_{\text{product}}/n_{\text{GUA}} \times 7)$  and was approximately 96%.

#### 4. Conclusions

We designed a BMZIF-decorated Mo carbide catalyst to develop a high-selectivity catalyst to produce phenols from HDO derived from guaiacol. When BMZIF was coated on the surface of the MoO<sub>3</sub> nanorods, BMZIF-generated metal oxide (ZnO and CoO) species dispersed on N-doped carbon shells, whereas the core MoO<sub>3</sub> nanorods were transformed into Mo<sub>2</sub>C. Different types of Mo<sub>2</sub>C@BMZIF core@shell nanorods were produced by controlling the carbonization temperature and time. The Mo<sub>2</sub>C@BMZIF-700 °C (4 h) catalyst produced by carbonization at 700 °C for 4 h, showed the highest guaiacol conversion (97%) and the highest phenol selectivity (70%) under the reaction condition of 330 °C, 4 h, 4 MPa using 60 mg of catalyst and 0.12 g of guaiacol in 20 mL *n*-decane. The improved catalytic performance of the Mo<sub>2</sub>C@BMZIF-700 °C (4 h) catalyst was attributed to the synergistic effect of the core Mo<sub>2</sub>C nanorod and the coated porous N-doped carbon shell containing highly dispersed ZnO and CoO species. It was found that the BMZIF shell generated the ZnO and CoO species in close contact with the Mo<sub>2</sub>C surface. The binding energy shift in the XPS profile demonstrated the charge transfer between the core Mo atom and the Zn and Co atoms of the shell consisting of N-doped carbon. The collective interaction of well-defined Mo, Co, and Zn metal atoms, as well as the N atom dispersed in the porous carbon, synergistically promotes the HDO performance of guaiacol with high phenol selectivity, which was not achieved by other supported catalysts. The Mo<sub>2</sub>C@BMZIF-700 °C (4 h) catalyst was also applied to the HDO reactions of syringol and vanillin as well as other lignin derivatives. The selective demethoxylation properties of Mo<sub>2</sub>C nanorods were further enhanced by the highly dispersed ZnO and CoO species on the porous N-doped carbon. The developed Mo<sub>2</sub>C@BMZIF catalyst has been proven to have excellent reusability and recyclability without changing the structure or active species. The unique core@shell structure of the Mo<sub>2</sub>C@BMZIF catalyst and its synergetic catalytic properties can be further applied to develop new HDO catalysts with high selective demethoxylation ability.

**Supplementary Materials:** The following supporting information can be downloaded at: <https://www.mdpi.com/article/10.3390/catal12121605/s1>, Figure S1: XRD of as-synthesized MoO<sub>3</sub> nanorods; Figure S2: TEM images of BMZIF-coated MoO<sub>3</sub> nanorods obtained by different calcination time at 700 °C under N<sub>2</sub> atmosphere: (a) 1, (b) 5, and (c) 24 h; Figure S3: A TEM image and corresponding elemental EDS maps of as-prepared MoO<sub>3</sub>@BMZIF nanorods without carbonization; Figure S4: N<sub>2</sub> adsorption-desorption isotherms of (a) as-prepared MoO<sub>3</sub>@BMZIF and (b) Mo<sub>2</sub>C@BMZIF-700 °C (4 h) core@shell nanorods; Figure S5: XPS profiles of Mo<sub>2</sub>C@BMZIF-700 °C (4 h) showing deconvoluted (a) Zn 2p and (b) Co 2p spectra; Figure S6: (a) A TEM image of Mo<sub>2</sub>C/Zn+Co-700 °C (4 h) and (b) XRD pattern of Mo+Co+Zn/AC catalyst; Table S1: Quantitative elemental analysis of ZIF-decorated Mo carbide nanorods with a core@shell structure by ICP-OES measurement; Table S2: Catalytic HDO results of syringol and vanillin over BMZIF@Mo<sub>2</sub>C-700 °C (4 h).

**Author Contributions:** Conceptualization, methodology, experiment, data curation, J.F.K.; analysis, data collection, visualization, J.F.K., S.L. and J.G.L.; writing—original draft preparation, J.F.K. and S.L.; supervision, funding acquisition, writing—review and editing, K.A. All authors have read and agreed to the published version of the manuscript.

**Funding:** This research was supported by the Basic Science Research Program (2021R1A2C2006713), the Engineering Research Center of Excellence Program (2020R1A5A1019631), the Climate Environment R&D Program (2022M3J1A1052840), the Regional Innovation Strategy (RIS) (2021RIS-003) of the National Research Foundation of Korea (NRF), funded by the Ministry of Science

and ICT, the Ministry of Education (MOE), and the Technology Innovation Program (20012971, 20010853) by the Ministry of Trade, Industry & Energy (MOTIE), and UNIST (1.220029.01).

**Acknowledgments:** This research was supported by the Basic Science Research Program (2021R1A2C2006713), the Engineering Research Center of Excellence Program (2020R1A5A1019631), the Climate Environment R&D Program (2022M3J1A1052840), the Regional Innovation Strategy (RIS) (2021RIS-003) of the National Research Foundation of Korea (NRF), funded by the Ministry of Science and ICT, the Ministry of Education (MOE), and the Technology Innovation Program (20012971, 20010853) by the Ministry of Trade, Industry & Energy (MOTIE), and UNIST (1.220029.01).

**Conflicts of Interest:** The authors declare no conflict of interest.

## References

1. Wong, S.S.; Shu, R.; Zhang, J.; Liu, H.; Yan, N. Downstream processing of lignin derived feedstock into end products. *Chem. Soc. Rev.* **2020**, *49*, 5510–5560. [[CrossRef](#)] [[PubMed](#)]
2. Bridgwater, A.V. Review of fast pyrolysis of biomass and product upgrading. *Biomass Bioenergy* **2012**, *38*, 68–94. [[CrossRef](#)]
3. Isikgor, F.H.; Becer, C.R. Lignocellulosic biomass: A sustainable platform for the production of bio-based chemicals and polymers. *Polym. Chem.* **2015**, *6*, 4497–4559. [[CrossRef](#)]
4. Tuck, C.O.; Pérez, E.; Horváth, I.T.; Sheldon, R.A.; Poliakoff, M. Valorization of biomass: Deriving more value from waste. *Science* **2012**, *337*, 695–699. [[CrossRef](#)] [[PubMed](#)]
5. Zakzeski, J.; Bruijninx, P.C.; Jongerius, A.L.; Weckhuysen, B.M. The catalytic valorization of lignin for the production of renewable chemicals. *Chem. Rev.* **2010**, *110*, 3552–3599. [[CrossRef](#)] [[PubMed](#)]
6. Schutyser, W.; Renders, A.T.; Van den Bosch, S.; Koelewijn, S.F.; Beckham, G.T.; Sels, B.F. Chemicals from lignin: An interplay of lignocellulose fractionation, depolymerisation, and upgrading. *Chem. Soc. Rev.* **2018**, *47*, 852–908. [[PubMed](#)]
7. Rinaldi, R.; Jastrzebski, R.; Clough, M.T.; Ralph, J.; Kennema, M.; Bruijninx, P.C.; Weckhuysen, B.M. Paving the way for lignin valorisation: Recent advances in bioengineering, biorefining and catalysis. *Angew. Chem. Int. Ed.* **2016**, *55*, 8164–8215. [[CrossRef](#)]
8. Ragauskas, A.J.; Beckham, G.T.; Biddy, M.J.; Chandra, R.; Chen, F.; Davis, M.F.; Wyman, C.E. Lignin valorization: Improving lignin processing in the biorefinery. *Science* **2014**, *344*, 1246843. [[CrossRef](#)]
9. Song, S.; Zhang, J.; Gözaydın, G.; Yan, N. Production of terephthalic acid from corn stover lignin. *Angew. Chem. Int. Ed.* **2019**, *58*, 4934–4937. [[CrossRef](#)]
10. Pang, J.; Zheng, M.; Sun, R.; Wang, A.; Wang, X.; Zhang, T. Synthesis of ethylene glycol and terephthalic acid from biomass for producing PET. *Green Chem.* **2016**, *18*, 342–359. [[CrossRef](#)]
11. Zhang, Y.; Naebe, M. Lignin: A review on structure, properties, and applications as a light-colored UV absorber. *ACS Sustain. Chem. Eng.* **2021**, *9*, 1427–1442. [[CrossRef](#)]
12. Terrell, E.; Dellon, L.D.; Dufour, A.; Bartolomei, E.; Broadbelt, L.J.; Garcia-Perez, M. A review on lignin liquefaction: Advanced characterization of structure and microkinetic modeling. *Ind. Eng. Chem. Res.* **2019**, *59*, 526–555. [[CrossRef](#)]
13. Saidi, M.; Samimi, F.; Karimipourfard, D.; Nimmanwudipong, T.; Gates, B.C.; Rahimpour, M.R. Upgrading of lignin-derived bio-oils by catalytic hydrodeoxygenation. *Energy Environ. Sci.* **2014**, *7*, 103–129. [[CrossRef](#)]
14. Alonso, D.M.; Bond, J.Q.; Dumesic, J.A. Catalytic conversion of biomass to biofuels. *Green Chem.* **2014**, *12*, 1493–1513. [[CrossRef](#)]
15. Fang, R.; Dhakshinamoorthy, A.; Li, Y.; Garcia, H. Metal organic frameworks for biomass conversion. *Chem. Soc. Rev.* **2020**, *49*, 3638–3687. [[CrossRef](#)]
16. Zhang, X.; Yan, P.; Zhao, B.; Liu, K.; Kung, M.C.; Kung, H.H.; Zhang, Z.C. Selective hydrodeoxygenation of guaiacol to phenolics by Ni/anatase TiO<sub>2</sub> catalyst formed by cross-surface migration of Ni and TiO<sub>2</sub>. *ACS Catal.* **2019**, *9*, 3551–3563. [[CrossRef](#)]
17. Lee, E.H.; Park, R.S.; Kim, H.; Park, S.H.; Jung, S.C.; Jeon, J.K.; Park, Y.K. Hydrodeoxygenation of guaiacol over Pt loaded zeolitic materials. *J. Ind. Eng. Chem.* **2016**, *37*, 18–21. [[CrossRef](#)]
18. Ishikawa, M.; Tamura, M.; Nakagawa, Y.; Tomishige, K. Demethoxylation of guaiacol and methoxybenzenes over carbon-supported Ru–Mn catalyst. *Appl. Catal. B* **2016**, *182*, 193–203. [[CrossRef](#)]
19. Liu, X.; Jia, W.; Xu, G.; Zhang, Y.; Fu, Y. Selective hydrodeoxygenation of lignin-derived phenols to cyclohexanols over Co-based catalysts. *ACS Sustain. Chem. Eng.* **2017**, *5*, 8594–8601. [[CrossRef](#)]
20. Furimsky, E. Catalytic hydrodeoxygenation. *Appl. Catal. A Gen.* **2000**, *199*, 147–190. [[CrossRef](#)]
21. Li, C.; Nakagawa, Y.; Tamura, M.; Nakayama, A.; Tomishige, K. Hydrodeoxygenation of guaiacol to phenol over ceria-supported iron catalysts. *ACS Catal.* **2020**, *10*, 14624–14639. [[CrossRef](#)]
22. Nowakowski, D.J.; Bridgwater, A.V.; Elliott, D.C.; Meier, D.; de Wild, P. Lignin fast pyrolysis: Results from an international collaboration. *J. Anal. Appl. Pyrolysis* **2010**, *88*, 53–72. [[CrossRef](#)]
23. McGhee, W.D. Selective Introduction of Active Sites for Hydroxylation of Benzene. U.S. Patent 5, 15 September 1998.
24. Lee, J.G.; Lee, S.; Lee, H.; Kurisingal, J.F.; Han, S.H.; Kim, Y.H.; An, K. Complete utilization of waste lignin: Preparation of lignin-derived carbon supports and conversion of lignin-derived guaiacol to nylon precursors. *Catal. Sci. Technol.* **2022**, *12*, 5021–5031. [[CrossRef](#)]
25. Mäki-Arvela, P.; Murzin, D.Y. Hydrodeoxygenation of lignin-derived phenols: From fundamental studies towards industrial applications. *Catalysts* **2017**, *7*, 265. [[CrossRef](#)]

26. Elliott, D.C.; Hart, T.R. Catalytic hydroprocessing of chemical models for bio-oil. *Energy Fuels* **2009**, *23*, 631–637. [[CrossRef](#)]
27. Gutierrez, A.; Kaila, R.K.; Honkela, M.L.; Slioor, R.; Krause, A.O.I. Hydrodeoxygenation of guaiacol on noble metal catalysts. *Catal. Today* **2009**, *147*, 239–246. [[CrossRef](#)]
28. Tran, N.T.; Uemura, Y.; Chowdhury, S.; Ramli, A. Vapor-phase hydrodeoxygenation of guaiacol on Al-MCM-41 supported Ni and Co catalysts. *Appl. Catal. A Gen.* **2016**, *512*, 93–100. [[CrossRef](#)]
29. Olcese, R.N.; Bettahar, M.; Petitjean, D.; Malaman, B.; Giovanella, F.; Dufour, A. Gas-phase hydrodeoxygenation of guaiacol over Fe/SiO<sub>2</sub> catalyst. *Appl. Catal. B* **2012**, *115*, 63–73. [[CrossRef](#)]
30. Lup, A.N.K.; Abnisa, F.; Daud, W.M.A.W.; Aroua, M.K. Synergistic interaction of metal–acid sites for phenol hydrodeoxygenation over bifunctional Ag/TiO<sub>2</sub> nanocatalyst. *Chin. J. Chem. Eng.* **2019**, *27*, 349–361. [[CrossRef](#)]
31. Bu, Q.; Lei, H.; Ren, S.; Wang, L.; Holladay, J.; Zhang, Q.; Ruan, R. Phenol and phenolics from lignocellulosic biomass by catalytic microwave pyrolysis. *Bioresour. Technol.* **2011**, *102*, 7004–7007. [[CrossRef](#)]
32. Moon, J.S.; Kim, E.G.; Lee, Y.K. Active sites of Ni<sub>2</sub>P/SiO<sub>2</sub> catalyst for hydrodeoxygenation of guaiacol: A joint XAFS and DFT study. *J. Catal.* **2014**, *311*, 144–152. [[CrossRef](#)]
33. Sulman, A.; Mäki-Arvela, P.; Bomont, L.; Alda-Onggar, M.; Fedorov, V.; Russo, V.; Murzin, D.Y. Kinetic and thermodynamic analysis of guaiacol hydrodeoxygenation. *Catal. Lett.* **2019**, *149*, 2453–2467. [[CrossRef](#)]
34. Engelhardt, J.; Lyu, P.; Nachtigall, P.; Schüth, F.; García, Á.M. The influence of water on the performance of molybdenum carbide catalysts in hydrodeoxygenation reactions: A combined theoretical and experimental study. *ChemCatChem* **2017**, *9*, 1985–1991. [[CrossRef](#)]
35. Ma, R.; Cui, K.; Yang, L.; Ma, X.; Li, Y. Selective catalytic conversion of guaiacol to phenols over a molybdenum carbide catalyst. *Chem. Comm.* **2015**, *51*, 10299–10301. [[CrossRef](#)] [[PubMed](#)]
36. Ma, R.; Hao, W.; Ma, X.; Tian, Y.; Li, Y. Catalytic ethanolsis of Kraft lignin into high-value small-molecular chemicals over a nanostructured  $\alpha$ -molybdenum carbide catalyst. *Angew. Chem.* **2014**, *126*, 7438–7443. [[CrossRef](#)]
37. Ghampson, I.T.; Sepúlveda, C.; Garcia, R.; Frederick, B.G.; Wheeler, M.C.; Escalona, N.; DeSisto, W.J. Guaiacol transformation over unsupported molybdenum-based nitride catalysts. *Appl. Catal. A Gen.* **2012**, *413*, 78–84. [[CrossRef](#)]
38. Jongerius, A.L.; Jastrzebski, R.; Bruijninx, P.C.; Weckhuysen, B.M. CoMo sulfide-catalyzed hydrodeoxygenation of lignin model compounds: An extended reaction network for the conversion of monomeric and dimeric substrates. *J. Catal.* **2012**, *285*, 315–323. [[CrossRef](#)]
39. Van, N.B.; Laurenti, D.; Delichère, P.; Geantet, C. Hydrodeoxygenation of guaiacol Part II: Support effect for CoMoS catalysts on HDO activity and selectivity. *Appl. Catal. B* **2021**, *101*, 246–255.
40. Zhou, M.; Ge, F.; Li, J.; Xia, H.; Liu, J.; Jiang, J.; Yang, X. Catalytic Hydrodeoxygenation of Guaiacol to Cyclohexanol over Bimetallic NiMo-MOF-Derived Catalysts. *Catalysts* **2022**, *12*, 371. [[CrossRef](#)]
41. Moreira, R.; Ochoa, E.; Pinilla, J.L.; Portugal, A.; Suelves, I. Liquid-phase hydrodeoxygenation of guaiacol over Mo<sub>2</sub>C supported on commercial CNF. Effects of operating conditions on conversion and product selectivity. *Catalysts* **2018**, *8*, 127. [[CrossRef](#)]
42. Prasomsri, T.; Shetty, M.; Murugappan, K.; Román-Leshkov, Y. Insights into the catalytic activity and surface modification of MoO<sub>3</sub> during the hydrodeoxygenation of lignin-derived model compounds into aromatic hydrocarbons under low hydrogen pressures. *Energy Environ. Sci.* **2014**, *7*, 2660–2669. [[CrossRef](#)]
43. Jongerius, A.L.; Gosselink, R.W.; Dijkstra, J.; Bitter, J.H.; Bruijninx, P.C.; Weckhuysen, B.M. Carbon nanofiber supported transition-metal carbide catalysts for the hydrodeoxygenation of guaiacol. *ChemCatChem* **2013**, *5*, 2964–2972. [[CrossRef](#)]
44. Chang, J.; Danuthai, T.; Dewiyanti, S.; Wang, C.; Borgna, A. Hydrodeoxygenation of Guaiacol over Carbon-Supported Metal Catalysts. *ChemCatChem* **2013**, *5*, 3041–3049. [[CrossRef](#)]
45. Cai, Z.; Wang, F.; Zhang, X.; Ahishakiye, R.; Xie, Y.; Shen, Y. Selective hydrodeoxygenation of guaiacol to phenolics over activated carbon supported molybdenum catalysts. *Mol. Catal.* **2017**, *441*, 28–34. [[CrossRef](#)]
46. Li, R.; Shahbazi, A.; Wang, L.; Zhang, B.; Hung, A.M.; Dayton, D.C. Graphite encapsulated molybdenum carbide core/shell nanocomposite for highly selective conversion of guaiacol to phenolic compounds in methanol. *Appl. Catal. A Gen.* **2016**, *528*, 123–130. [[CrossRef](#)]
47. Ghampson, I.T.; Sepúlveda, C.; Garcia, R.; Radovic, L.R.; Fierro, J.G.; DeSisto, W.J.; Escalona, N. Hydrodeoxygenation of guaiacol over carbon-supported molybdenum nitride catalysts: Effects of nitriding methods and support properties. *Appl. Catal. A Gen.* **2012**, *439*, 111–124. [[CrossRef](#)]
48. Sepúlveda, C.; Leiva, K.; García, R.; Radovic, L.R.; Ghampson, I.T.; DeSisto, W.J.; Escalona, N. Hydrodeoxygenation of 2-methoxyphenol over Mo<sub>2</sub>N catalysts supported on activated carbons. *Catal. Today* **2011**, *172*, 232–239. [[CrossRef](#)]
49. Baddour, F.G.; Witte, V.A.; Nash, C.P.; Griffin, M.B.; Ruddy, D.A.; Schaidle, J.A. Late-transition-metal-modified  $\beta$ -Mo<sub>2</sub>C catalysts for enhanced hydrogenation during guaiacol deoxygenation. *ACS Sustain. Chem. Eng.* **2017**, *5*, 11433–11439. [[CrossRef](#)]
50. Griboval-Constant, A.; Giraudon, J.M.; Leclercq, G.; Leclercq, L. Catalytic behaviour of cobalt or ruthenium supported molybdenum carbide catalysts for FT reaction. *Appl. Catal. A Gen.* **2004**, *260*, 35–45. [[CrossRef](#)]
51. Lewandowski, M.; Szymańska-Kolasa, A.; Da Costa, P.; Sayag, C. Catalytic performances of platinum doped molybdenum carbide for simultaneous hydrodenitrogenation and hydrodesulfurization. *Catal. Today* **2007**, *119*, 31–34. [[CrossRef](#)]
52. Schweitzer, N.M.; Schaidle, J.A.; Ezekoye, O.K.; Pan, X.; Linic, S.; Thompson, L.T. High activity carbide supported catalysts for water gas shift. *J. Am. Chem. Soc.* **2011**, *133*, 2378–2381. [[CrossRef](#)]

53. Schaidle, J.A.; Lausche, A.C.; Thompson, L.T. Effects of sulfur on Mo<sub>2</sub>C and Pt/Mo<sub>2</sub>C catalysts: Water gas shift reaction. *J. Catal.* **2010**, *272*, 235–245. [[CrossRef](#)]
54. Perret, N.; Wang, X.; Delannoy, L.; Potvin, C.; Louis, C.; Keane, M.A. Enhanced selective nitroarene hydrogenation over Au supported on β-Mo<sub>2</sub>C and β-Mo<sub>2</sub>C/Al<sub>2</sub>O<sub>3</sub>. *J. Catal.* **2012**, *286*, 172–183. [[CrossRef](#)]
55. Xiang, M.; Li, D.; Xiao, H.; Zhang, J.; Li, W.; Zhong, B.; Sun, Y. K/Ni/β-Mo<sub>2</sub>C: A highly active and selective catalyst for higher alcohols synthesis from CO hydrogenation. *Catal. Today* **2008**, *131*, 489–495. [[CrossRef](#)]
56. Chakraborty, G.; Park, I.H.; Medishetty, R.; Vittal, J.J. Two-dimensional metal-organic framework materials: Synthesis, structures, properties and applications. *Chem. Rev.* **2021**, *121*, 3751–3891. [[CrossRef](#)]
57. Herbst, A.; Janiak, C. MOF catalysts in biomass upgrading towards value-added fine chemicals. *Cryst. Eng. Comm.* **2017**, *19*, 4092–4117. [[CrossRef](#)]
58. Liao, Y.T.; Matsagar, B.M.; Wu, K.C.W. Metal-organic framework (MOF)-derived effective solid catalysts for valorization of lignocellulosic biomass. *ACS Sustain. Chem. Eng.* **2018**, *6*, 13628–13643. [[CrossRef](#)]
59. Xia, B.Y.; Yan, Y.; Li, N.; Wu, H.B.; Lou, X.W.D.; Wang, X. A metal-organic framework-derived bifunctional oxygen electrocatalyst. *Nat. Energy* **2016**, *1*, 15006. [[CrossRef](#)]
60. Zhou, H.C.; Long, J.R.; Yaghi, O.M. Introduction to metal-organic frameworks. *Chem. Rev.* **2012**, *112*, 673–674. [[CrossRef](#)]
61. Deng, Y.; Dong, Y.; Wang, G.; Sun, K.; Shi, X.; Zheng, L.; Liao, S. Well-defined ZIF-derived Fe-N codoped carbon nanoframes as efficient oxygen reduction catalysts. *ACS Appl. Mater. Interfaces* **2017**, *9*, 9699–9709. [[CrossRef](#)]
62. Xu, Y.; Shan, W.; Liang, X.; Gao, X.; Li, W.; Li, H.; Qiu, X. Cobalt nanoparticles encapsulated in nitrogen-doped carbon shells: Efficient and stable catalyst for nitrobenzene reduction. *Ind. Eng. Chem. Res.* **2020**, *59*, 4367–4376. [[CrossRef](#)]
63. Zhou, K.; Mousavi, B.; Luo, Z.; Phatanasri, S.; Chaemchuen, S.; Verpoort, F. Characterization and properties of Zn/Co zeolitic imidazolate frameworks vs. ZIF-8 and ZIF-67. *J. Mater. Chem. A* **2017**, *5*, 952–957. [[CrossRef](#)]
64. Chen, Y.Z.; Wang, C.; Wu, Z.Y.; Xiong, Y.; Xu, Q.; Yu, S.H.; Jiang, H.L. From bimetallic metal-organic framework to porous carbon: High surface area and multicomponent active dopants for excellent electrocatalysis. *Adv. Mater.* **2015**, *27*, 5010–5016. [[CrossRef](#)]
65. Huang, M.; Mi, K.; Zhang, J.; Liu, H.; Yu, T.; Yuan, A.; Xiong, S. MOF-derived bi-metal embedded N-doped carbon polyhedral nanocages with enhanced lithium storage. *J. Mater. Chem. A* **2017**, *5*, 266–274. [[CrossRef](#)]
66. Lee, J.G.; Yoon, S.; Yang, E.; Lee, J.H.; Song, K.; Moon, H.R.; An, K. Structural evolution of ZIF-67-derived catalysts for furfural hydrogenation. *J. Catal.* **2020**, *392*, 302–312. [[CrossRef](#)]
67. Tian, W.; Hu, H.; Wang, Y.; Li, P.; Liu, J.; Liu, J.; Wu, M. Metal-organic frameworks mediated synthesis of one-dimensional molybdenum-based/carbon composites for enhanced lithium storage. *ACS Nano* **2018**, *12*, 1990–2000. [[CrossRef](#)]
68. Ma, F.X.; Wu, H.B.; Xia, B.Y.; Xu, C.Y.; Lou, X.W. Hierarchical β-Mo<sub>2</sub>C nanotubes organized by ultrathin nanosheets as a highly efficient electrocatalyst for hydrogen production. *Angew. Chem. Int. Ed.* **2015**, *54*, 15395–15399. [[CrossRef](#)]
69. Qi, B.; Ni, X.; Li, D.; Zheng, H. A facile non-hydrothermal fabrication of uniform α-MoO<sub>3</sub> nanowires in high yield. *Chem. Lett.* **2008**, *37*, 336–337. [[CrossRef](#)]
70. Reddy, C.V.S.; Walker Jr, E.H.; Wen, C.; Mho, S.I. Hydrothermal synthesis of MoO<sub>3</sub> nanobelts utilizing poly (ethylene glycol). *J. Power Sources* **2008**, *183*, 330–333. [[CrossRef](#)]
71. Li, W.; Cheng, F.; Tao, Z.; Chen, J. Vapor-transportation preparation and reversible lithium intercalation/deintercalation of α-MoO<sub>3</sub> microrods. *J. Phys. Chem. B* **2006**, *110*, 119–124. [[CrossRef](#)]
72. Tri, T.M.; Candy, J.P.; Gallezot, P.; Massardier, J.; Prlmet, M.; Vadrine, J.C.; Imelik, B. PtMo bimetallic catalysts supported on Y-zeolite: I. Characterization of the catalysts. *J. Catal.* **1983**, *79*, 396–409. [[CrossRef](#)]
73. Tokarz-Sobieraj, R.; Hermann, K.; Witko, M.; Blume, A.; Mestl, G.; Schlögl, R. Properties of oxygen sites at the MoO<sub>3</sub> (010) surface: Density functional theory cluster studies and photoemission experiments. *Surf. Sci.* **2001**, *489*, 107–125. [[CrossRef](#)]
74. Chen, J.S.; Cheah, Y.L.; Madhavi, S.; Lou, X.W. Fast synthesis of α-MoO<sub>3</sub> nanorods with controlled aspect ratios and their enhanced lithium storage capabilities. *J. Phys. Chem. C* **2010**, *114*, 8675–8678. [[CrossRef](#)]
75. Zhong, H.X.; Wang, J.; Zhang, Y.W.; Xu, W.L.; Xing, W.; Xu, D.; Zhang, X.B. ZIF-8 derived graphene-based nitrogen-doped porous carbon sheets as highly efficient and durable oxygen reduction electrocatalysts. *Angew. Chem. Int. Ed.* **2014**, *53*, 14235–14239. [[CrossRef](#)] [[PubMed](#)]
76. Wang, B.; Wang, G.; Wang, H. Hybrids of Mo<sub>2</sub>C nanoparticles anchored on graphene sheets as anode materials for high performance lithium-ion batteries. *J. Mater. Chem. A* **2015**, *3*, 17403–17411. [[CrossRef](#)]
77. Smyth, C.M.; Addou, R.; McDonnell, S.; Hinkle, C.L.; Wallace, R.M. Contact metal-MoS<sub>2</sub> interfacial reactions and potential implications on MoS<sub>2</sub>-based device performance. *J. Phys. Chem. C* **2016**, *120*, 14719–14729. [[CrossRef](#)]
78. Oshikawa, K.; Nagai, M.; Omi, S. Characterization of molybdenum carbides for methane reforming by TPR, XRD, and XPS. *J. Phys. Chem. B* **2001**, *105*, 9124–9131. [[CrossRef](#)]
79. Ledoux, M.J.; Huu, C.P.; Guille, J.; Dunlop, H. Compared activities of platinum and high specific surface area Mo<sub>2</sub>C and WC catalysts for reforming reactions: I. Catalyst activation and stabilization: Reaction of n-hexane. *J. Catal.* **1992**, *134*, 383–398. [[CrossRef](#)]
80. Kumar, P.; Singh, M.; Reddy, G.B. Oxidized core-shell MoO<sub>2</sub>-MoS<sub>2</sub> nanostructured thin films for hydrogen evolution. *ACS Appl. Nano Mater.* **2019**, *3*, 711–723. [[CrossRef](#)]
81. Li, P.; Liu, J.; Wang, Y.; Liu, Y.; Wang, X.; Nam, K.W.; Qiu, J. Synthesis of ultrathin hollow carbon shell from petroleum asphalt for high-performance anode material in lithium-ion batteries. *Chem. Eng. J.* **2016**, *286*, 632–639. [[CrossRef](#)]



82. Murugappan, K.; Anderson, E.M.; Teschner, D.; Jones, T.E.; Skorupska, K.; Román-Leshkov, Y. Operando NAP-XPS unveils differences in MoO<sub>3</sub> and Mo<sub>2</sub>C during hydrodeoxygenation. *Nat. Catal.* **2018**, *1*, 960–967. [[CrossRef](#)]
83. Zhong, M.; Yang, D.; Xie, C.; Zhang, Z.; Zhou, Z.; Bu, X.H. Yolk-Shell MnO@ZnMn<sub>2</sub>O<sub>4</sub>/N-C Nanorods Derived from  $\alpha$ -MnO<sub>2</sub>/ZIF-8 as Anode Materials for Lithium Ion Batteries. *Small* **2016**, *12*, 5564–5571. [[CrossRef](#)]
84. Wang, X.; Zhu, S.; Wang, S.; He, Y.; Liu, Y.; Wang, J.; Lv, Y. Low temperature hydrodeoxygenation of guaiacol into cyclohexane over Ni/SiO<sub>2</sub> catalyst combined with H $\beta$  zeolite. *RSC Adv.* **2019**, *9*, 3868–3876. [[CrossRef](#)]
85. Venkatesan, K.; Krishna, J.J.; Anjana, S.; Selvam, P.; Vinu, R. Hydrodeoxygenation kinetics of syringol, guaiacol and phenol over H-ZSM-5. *Catal. Commun.* **2021**, *148*, 106164. [[CrossRef](#)]
86. Jiang, Z.; Zhang, W.; Jin, L.; Yang, X.; Xu, F.; Zhu, J.; Huang, W. Direct XPS evidence for charge transfer from a reduced rutile TiO<sub>2</sub> (110) surface to Au clusters. *J. Phys. Chem. C* **2007**, *111*, 12434–12439. [[CrossRef](#)]
87. Tran, C.C.; Han, Y.; Garcia-Perez, M.; Kaliaguine, S. Synergistic effect of Mo–W carbides on selective hydrodeoxygenation of guaiacol to oxygen-free aromatic hydrocarbons. *Catal. Sci. Technol.* **2019**, *9*, 1387–1397. [[CrossRef](#)]
88. Liu, X.; Song, Y.; Geng, W.; Li, H.; Xiao, L.; Wu, W. Cu-Mo<sub>2</sub>C/MCM-41: An efficient catalyst for the selective synthesis of methanol from CO<sub>2</sub>. *Catalysts* **2016**, *6*, 75. [[CrossRef](#)]
89. Kurisingal, J.F.; Babu, R.; Kim, S.H.; Li, Y.X.; Chang, J.S.; Cho, S.J.; Park, D.W. Microwave-induced synthesis of a bimetallic charge-transfer metal organic framework: A promising host for the chemical fixation of CO<sub>2</sub>. *Catal. Sci. Technol.* **2018**, *8*, 591–600. [[CrossRef](#)]
90. Velicky, M.; Donnelly, G.E.; Hendren, W.R.; McFarland, S.; Scullion, D.; DeBenedetti, W.J.; Huang, F. Mechanism of gold-assisted exfoliation of centimeter-sized transition-metal dichalcogenide monolayers. *ACS Nano* **2018**, *12*, 10463–10472. [[CrossRef](#)]
91. Blanco, E.; Sepulveda, C.; Cruces, K.; García-Fierro, J.L.; Ghampson, I.T.; Escalona, N. Conversion of guaiacol over metal carbides supported on activated carbon catalysts. *Catal. Today* **2020**, *356*, 376–383. [[CrossRef](#)]